Int. J. Electrochem. Sci., 17 **(2022)** Article Number: 220728, doi: 10.20964/2022.07.33

International Journal of
ELECTROCHEMICAL
SCIENCE
www.electrochemsci.org

Investigation on Effect of Temperature Alternation on Mechanical Properties of Embedded Reinforcements in Rammed Earth

Hao Chen, Xue Pan

Wuhan City Polytechnic, Hubei Wuhan, 430072, China
*E-mail: Wu_chen0072@163.com

Received: 7 March 2022 / *Accepted:* 25 April 2022 / *Published:* 6 June 2022

The mechanical properties of embedded reinforcement seriously affect the stability of rammed earth. However, more researches was focused on to analyze the mechanical properties of rammed earth to put forward improvement measures, but there were few studies on the impact of embedded reinforcement in rammed earth. In this paper, the effect of temperature alternation on mechanical properties of embedded reinforcements in rammed earth was investigated through microscopic morphology analysis and electrochemical experiments. The results showed that with the increase of the cycles, the mechanical parameters (including yield strength, tensile strength, section shrinkage and elongation rate) all decreased, and the mechanism characteristics of 20MnSi steel changed from plastic to brittle at T_c = 30 cycles. The corrosion current density increased rapidly from 6.29×10^{-3} A/m^2 (T_c = 20 cycles) to 62.84×10^{-3} A/m^2 (T_c = 30 cycles), and then basically remains unchanged, while the cathodic process changed from oxygen diffusion control to activation control. This is because temperature alternation destroyed the mesh skeleton structure of 20MnSi steel, and 20MnSi steel precipitated the second phase mainly composed of Ni and Cr element, which caused decreasing corrosion resistance and plastic of 20MnSi steel.

Keywords: Temperature alternation; Mechanical properties; 20MnSi steel; Rammed earth

1. INTRODUCTION

Rammed earth building is one of the historical building forms built from local materials. It has the advantages of low energy consumption, low cost and low maintenance cost. Besides, the materials used in rammed earth building are easy to obtain, pollution-free and highly recyclable. In the new rammed earth structure, the embedded reinforcement can effectively increase the mechanical properties of the rammed earth wall [1-3]. However, the rammed earth wall will shrink to a certain

extent when it is used for a long time, and the salt corrosion resistance is poor, which has a great influence on the mechanical properties of the embedded reinforcement [2,4].

For one aspect, relevant scholars have studied the improvement of soil performance under different test conditions. Zhou et al. [5] maintained the cube specimen at temperature of 30-50℃ and humidity of 55%-60% to observe the failure mode of the modified specimen in the compressive strength test, and then obtained the law between curing time and compressive strength. After adding cement and jute, Villacreses et al. [6] studied the law of water transfer of the modified material in a humid environment, and discussed the mechanical properties of the material in unconventional test environments such as freeze-thaw, dry-wet and so on.

For the other aspect, some scholars have studied the mechanical properties of reinforcement under different temperatures in rammed earth. Nguyen et al. [7] studied the temperature stress of rammed earth structures through experiments, and finally concluded that reinforced rammed earth structures would produce great deformation, cracks and stress under thermal loads such as temperature and solar radiation. Romanazzi et al. [8] studied the early cracking state of reinforced rammed earth structures by numerical simulation based on A three-dimensional thermodynamic model. Xie et al. [9] simulated and analyzed the early cracking behavior of reinforced rammed earth structures by using finite difference finite element method, considering the shrinkage and creep of concrete and external environment. Martín-del-Rio et al. [10] thought the nonlinear behavior of reinforced rammed earth structures was mainly temperature shrinkage creep strain and different materials of the cause, by considering the impact of these factors, the development situation of thermodynamics for early damage finite element analysis, to calculate the stress distribution of this kind of condition.

However, the above studies mainly analyzed the mechanical properties of rammed earth through experimental and numerical simulation methods, and put forward a series of improvement measures [5-10], but there were few studies on the impact of embedded reinforcement in rammed earth [11,12]. Therefore, this paper focused on the stress effect of rammed earth on embedded reinforcements due to the temperature alternation, and carries out research through microscopic morphology analysis and electrochemical experiments.

2. EXPERIMENTAL SETTINGS

The test soil sample was loose and in small clumps. After the soil was retrieved, the root, stem, leaf, brick, tile, stone and other impurities in the soil were all removed. If the granular degree of plain soil sample was obvious, it needed to be broken to ensure that the maximum particle size of soil particles did not exceed 2.0 mm. The water content of soil sample was 21.3%.

In this paper, 20MnSi steel with high strength and good comprehensive performance was adopted as the research object, and its main components were shown in Table 1.

Table 1. The main component of 20MnSi steel (mass fraction, wt.%)

Element	C	Mn	Ni	Si	Cr	Fe
wt.%	0.19	1.43	0.028	0.49	0.026	Balance

Based on the standards of GB/T 50123 "Standard for soil test method" and GB/T 50081 "Standard for test method of mechanical properties on ordinary concrete", the rammed earth sample was prepared by cubic steel die with side length of 150 mm [13].

The rammed earth sample was made by ramming forming scheme, which was divided into three layers for tamping, and each layer was rammed until no obvious soil sank. The chisel treatment was used between layers, and the 20MnSi steel was embedded in the second layer, as shown in Figure 1. After the specimen was finished, it was released from the mold, and the quantity and height of the sample was measured to ensure that the density of each specimen was 2.1-2.2×10^3 g/cm^3. After demudging, put the sample into a plastic bag, drain the air in the bag and tie the bag tightly for marking to ensure that the sample did not lose water [13,14].

During the experiment, the prepared sample with 20MnSi steel was put into the experimental device as shown in Figure 2, and the experimental rammed earth was compacted through the cover plate to ensure the tightness and non-deformation of the experimental device. The inner surface of the experimental box was made of iron, the outer surface was set with an insulating layer, and the thermocouple was set in the middle to control the temperature.

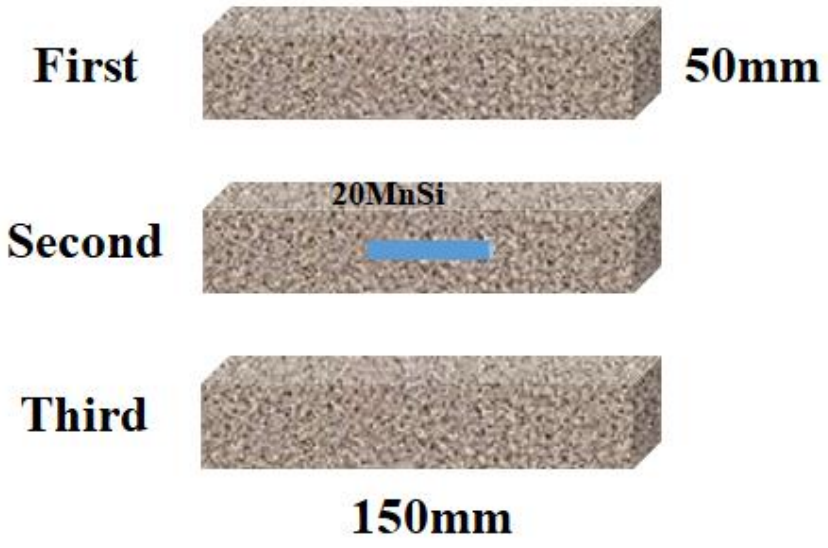

Figure 1. The structure of three-layer remmed earth sample embedded with 20MnSi steel

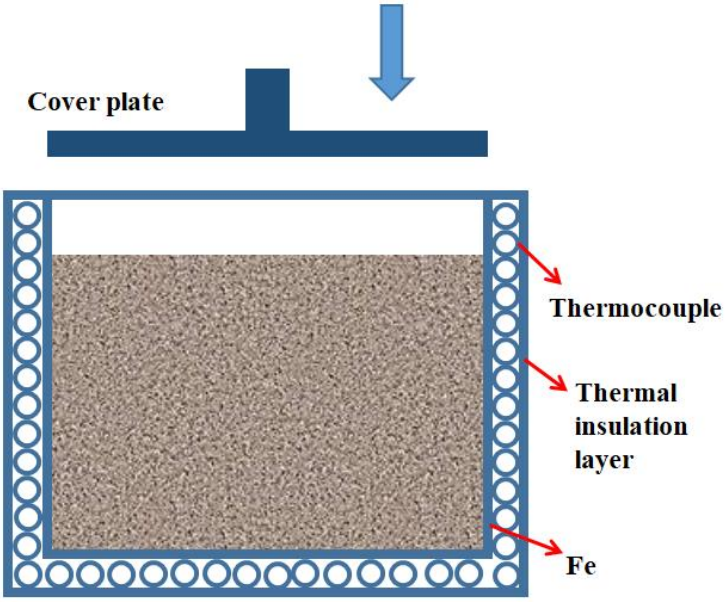

Figure 2. The experimental device for applying alternating temperature in different cycles

In this paper, the accelerated test method was adopted. The temperature range was set as 15-30℃, the heating/cooling rate was set as 1℃/10min, and the 50 cycles were carried out. The samples were taken out for slow strain rate tensile (SSRT) test and electrochemical test in different temperature-alternating cycles, respectively. At the end of the 50th cycle, SEM metallographic analysis and EDS surface scanning analysis were carried out.

SSRT experiment was used to measure the stress-strain curves of 20MnSi steel under different temperature-alternating cycles. The test samples were prepared according to GB/T 228 "Metallic materials – Tensile testing at ambient temperature". Smooth cylindrical specimens were used, with working section diameter of 5 mm and standard distance of 30 mm. Before the experiment, ensure that the sample has no defects, and then remove oil, dry after polishing. The SSRT experiment was carried out with the strain rate of 1×10^{-6} s^{-1} under different temperature-alternating cycles [13-16].

Electrochemical experiments were conducted to analyze the corrosion kinetics characteristics of 20MnSi steel at different temperature-alternating cycles. The sample size was $10\times10\times2$ mm^3. Before the experiment, the samples were cleaned with acetone, deionized water and anhydrous ethanol successively and then dried. The samples were polished with metallographic sandpaper until no obvious scratches on their surfaces and then polished. After the experiment, the sample was taken out and the solid particles on the surface were cleaned for electrochemical testing. A three-electrode system was used in the experiment. The auxiliary electrode was platinum electrode, the reference electrode was saturated calomel electrode, and the working electrode was 20MnSi steel after temperature-alternating experiment. The analytical pure reagent and deionized water were used to configure an experimental solution with a mass fraction of 3%. The ionic composition was shown in Table 2. The experimental temperature was set at 25℃.

Table 2. The ionic composition of experimental solution for electrochemical test

Component	$CaCl_2$	NaCl	Na_2SO_4	$MgSO_4 \cdot 7H_2O$	KNO_3	$NaHCO_3$
Content /(g/L)	0.111	0.468	0.142	0.197	0.293	0.151

3. RESULTS AND DISCUSSION

3.1 Stress-strain experiment

Figure 3 showed the changes of stress-strain curves and mechanical parameters, including yield strength (σ_s), tensile strength (σ_b), elongation rate (δ) and section shrinkage (ψ), of 20MnSi steel at different temperature-alternating cycles (T_c). Table 3 presented the fitting equations of mechanical parameters and temperature-alternating cycles. As can be seen from the Figure, a trend of 20MnSi steel was shown from elastic deformation to plastic deformation under different temperature-alternating periods, and the elastic deformation zones of 20MnSi steel under different cycles basically coincided. With the increase of the cycles, the yield strength and tensile strength decreased exponentially, the section shrinkage decreased linearly, and the elongation rate decreased slowly at first and then rapidly, showing a quadratic function change lawn, as shown in Table 3. For the original 20MnSi steel, the tensile strength was 410 MPa and the yield strength was 245 MPa. In this paper, the tensile strength and yield strength of 20MiSi steel were 232.8 MPa and 242.3 MPa respectively at T_c = 5 cycles and the difference between them decreased rapidly, from 165 MPa to 9.5 MPa. With the increase of cycles, the tensile strength and yield strength of 20MiSi steel all decreased synchronously in the form of power exponent. At the same time, after passing the deformation point, the strength of 20MnSi steel decreased rapidly at the necking stage and then fracture occurred. It should be noted that there was no obvious yield stage in stress-strain curve of 20MnSi steel at T_c = 10 and 20 cycles. However, at T_c = 30-50 cycles, there were obvious yield stages in the stress-strain curve, indicating that the mechanism characteristics of 20MnSi steel changed from plastic to brittle at this time [17]. Therefore, the increase of temperature-alternating cycles had no effect on the elastic deformation stage of 20MnSi steel, but will reduce the yield strength and tensile strength of the material, and increased the brittleness of 20MnSi steel.

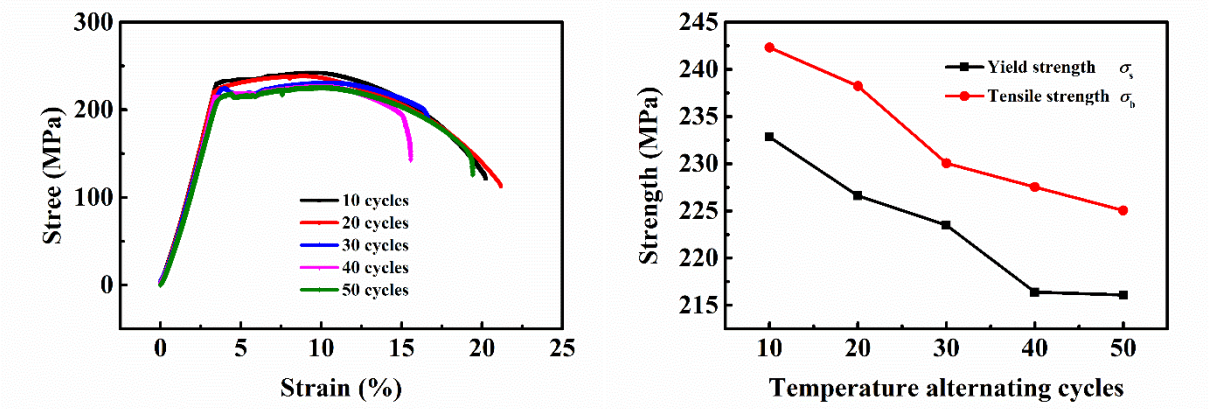

(1) Stress-strain curve (2) Yield strength (σ_s) and Tensile strength (σ_b)

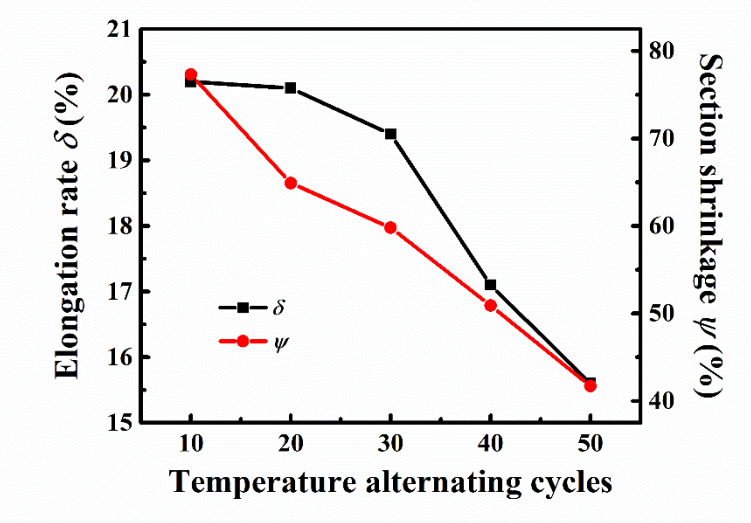

(3) Elongation rate (δ) and Section shrinkage (ψ)

Figure 3. The changes of stress-strain curves and mechanical parameters, including yield strength (σ_s), tensile strength (σ_b), elongation rate (δ) and section shrinkage (ψ), of 20MnSi steel at different temperature-alternating cycles (T_c = 10-50 cycles) in the range of 15-30 ℃ with the heating/cooling rate of 1℃/10min

Table 3. The fitted equations of mechanical parameters and temperature-alternating cycles

Parameter	Fitting equation	R^2
Yield strength	$\sigma_s = 261.38 \cdot T_c^{-0.049}$	0.95
Tensile strength	$\sigma_b = 272.17 \cdot T_c^{-0.048}$	0.96
Elongation rate	$\delta = -0.0031 \cdot (T_c - 10.742)^2 + 19.758$	0.98
Section shrinkage	$\Psi = -0.852 \cdot T_c + 84.48$	0.99

3.2 Microscope morphology and EDS analysis

Figure 4 showed the microscopic morphology of the 20MnSi steel with or without 50 cycles of temperature alternation. As can be seen from the Figure 4(1), with 200-times magnification in 50 μm, the microstructure of the original 20MnSi sample was elongated and continuous dendritic crystal structure, with good connection between different phases and high tensile strength. Furthermore, the morphology with local magnification of 500 times in 20 μm, the dendritic structure was arranged longitudinally, and the elongated dendritic structure had a high continuity. Significantly, there were connections between the elongated dendritic structures arranged lengthways, which further formed a network skeleton structure, as shown in the microscope with the amplification of 800 times in 12.5 μm. Therefore, the original 20MnSi steel without the influence of temperature-alternating cycles had high yield strength and tensile strength, showing good mechanical properties [18]. However, after treated by the 50 cycles of temperature alternation, the original skeleton structure was not obvious in the microscopic morphology magnified 200 times in Figure 4(2), showing a chain structure, and the connection between different phases no longer existed. More clearly in 20 μm, the 20MnSi steel had

become a uniform miscible structure, and the original skeleton structure had been destroyed. Moreover, the second phase precipitated on the microscopic surface of 20MnSi steel, proved by the microscopic morphology in 12.5 μm.

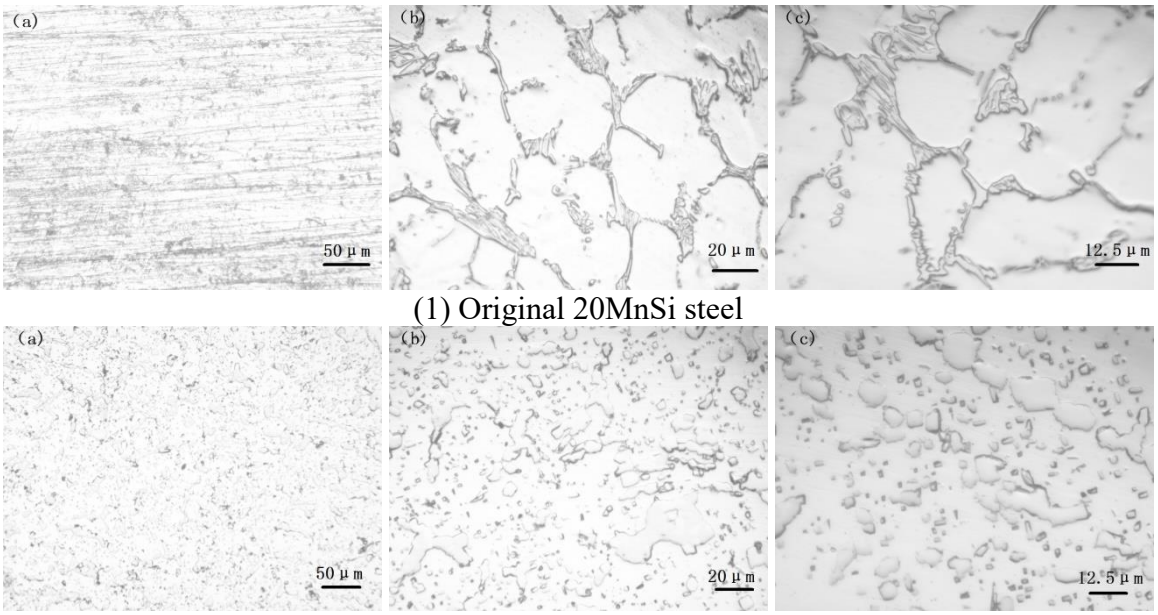

(1) Original 20MnSi steel

(2) 20MnSi steel at T_c = 50 cycles

Figure 4. The microscopic morphology of affected and unaffected 20MnSi steel

The composition of 20MnSi steel after 50 cycles of temperature alternation was analyzed by EDS analysis, as shown in Figure 5. It can be seen that the precipitated second phase was mainly Cr and Ni elements, followed by Fe element, while C, Mn and Si elements were basically not precipitated. As well-known, Cr and Ni elements were two kinds of metal elements with good ductility [19].

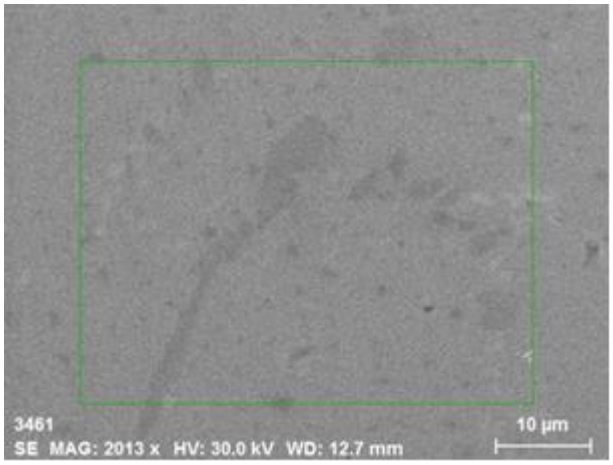

(1) Microscopic morphology of the EDS scanned area

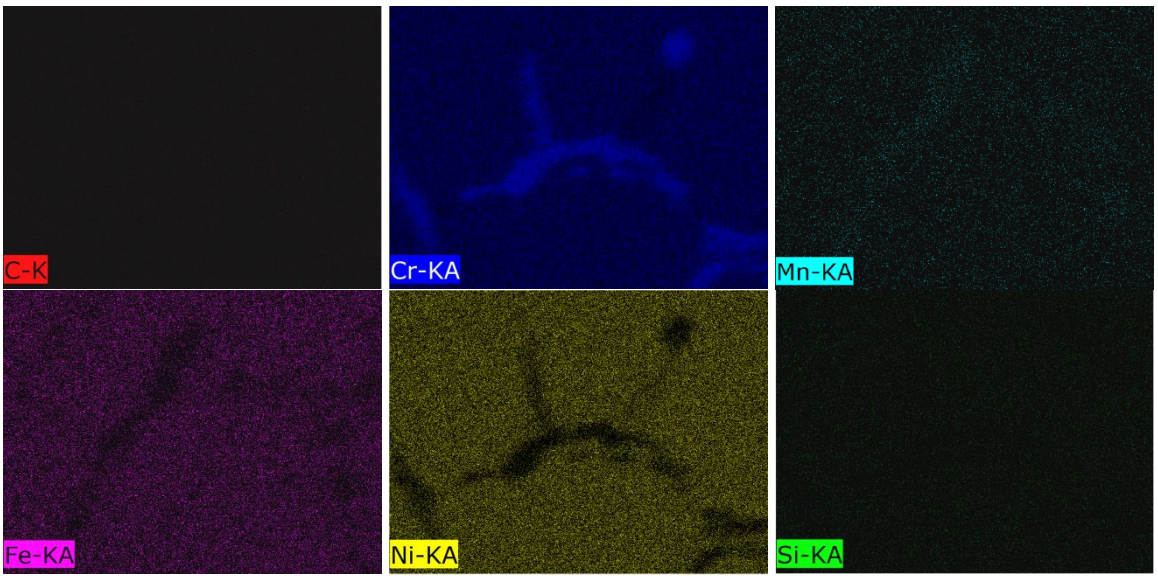

(2) Precipitated element distribution

Figure 5. The EDS analysis of the 20MnSi steel at T_c = 50 cycles

Under the influence of temperature alternation, a large number of these two elements precipitated out as the second phase, which destroyed the skeleton structure of the original 20MnSi steel and led to the increase of brittleness of 20MnSi steel.

3.3 Electrochemical test

Figure 6 showed the electrochemical curves including polarization curves and EIS curves of 20MnSi steel under the conditions of T_c = 10-50 cycles in 3 wt.% NaCl solution at 25℃. Table 4 presented the fitted results of polarization curves of 20MnSi steel under different temperature-alternating cycles. Figure 7 shoed the changes of different EIS parameters, including system capacitance (Q), double-layer capacitance (C_{dl}), surface resistance (R_p), Warsburg resistance (W) and charger transfer resistance (R_{ct}), with temperature-alternating cycles, and Table 5 presented the fitted equations of electrochemical parameters and temperature-alternating cycles.

It can be seen from the polarization curves that as the temperature-alternating cycle increased, the polarization curve of 20MiSi steel moved downward to the right, indicating that the temperature-alternating cycle increased the corrosion rate of the metal. Much more in detail, the anodic polarization curves in different cycles were significantly similar in shape, and the Tafel constant (b_a) with an average value of 66 mV/dec basically remained unchanged, indicating that the temperature alternation had no influence on corrosion mechanism and apparent corrosion rate of anodic reaction. This was mainly because, under the influence of temperature alternation, a large number of Cr and Ni elements were precipitated as shown in Figure 5, so as to that the protective film such as CrO_3 cannot be effectively formed on the surface of 20MnSi steel. Therefore, 20MnSi steel gradually degraded and formed properties similar to carbon steel [20,21]. Under this circumstance, the Fe base was always exposed in the corrosion environment with a basically same apparent anodic corrosion rate [20-25].

However, from the aspect of corrosion current density (I_{corr}), it can be seen that the I_{corr} increased rapidly from 0.02×10^{-3} A/m^2 (T_c = 10 cycles) to 62.84×10^{-3} A/m^2 (T_c = 30 cycles), and then basically remained unchanged with the average value of 63.34×10^{-3} A/m^2, which notably stated an increasing corrosion rate [26-31].

Focused on the cathodic polarization curves of 20MnSi steel, it changed greatly, presenting that the cathodic Tafel constant (b_c) decreased gradually [32], and the oxygen diffusion control section in the cathodic zone disappeared, changing to activation control [33-35]. Combined with the Figure 4 and Figure 5, the temperature alternation had a great influence on the structure of the 20MiSi steel, illustrating that the Cr and Ni elements precipitated and the original skeleton structure was destroyed. Under this condition, the Fe in grain boundaries worked as anode, and the independent gains acted as cathode, in which the intergranular corrosion rate was depended on the number of independent gains. Therefore, the increase of I_{corr} was caused by the non-Faraday process in different phases, presented a variable b_c.

Under different temperature-alternating cycles, the EIS curves of 20MnSi steel showed the characteristics of double capacitance-arc resistance, which indicated that there were two time constants in the whole experimental system, namely, the charge transfer process at low-frequency, and the mass transfer process at high-frequency [36,37]. Therefore, its equivalent circuit was chosen as $R_s(Q(R_pW(C_{dl}R_{ct})))$, including solution resistance (R_s), constant phase Angle element (Q), surface resistance (R_p), Warburg impedance (W), double-layer capacitance (C_{dl}) and charge transfer resistance (R_{ct}). With the increase of temperature-alternating cycles, the capacitance (Q) decreased gradually, while the double-layer capacitance (C_{dl}) increased gradually. In contrast, the surface resistance (R_p), Warburg impedance (W) and charge transfer resistance (R_{ct}) all decreased [29,34]. This was because with the increase of the temperature-alternating cycles, 20MnSi steel precipitated the second phase mainly composed of Ni and Cr element, which significantly reduced the corrosion resistance and formed loose and porous corrosion products. Therefore, its capacitance (Q) and surface resistance (R_p) gradually decreased. At the same time, due to the action of stress, the charge transfer process was promoted [31], so the double-layer capacitance (C_{dl}) increased with a deceasing charge transfer resistance (R_{ct}).

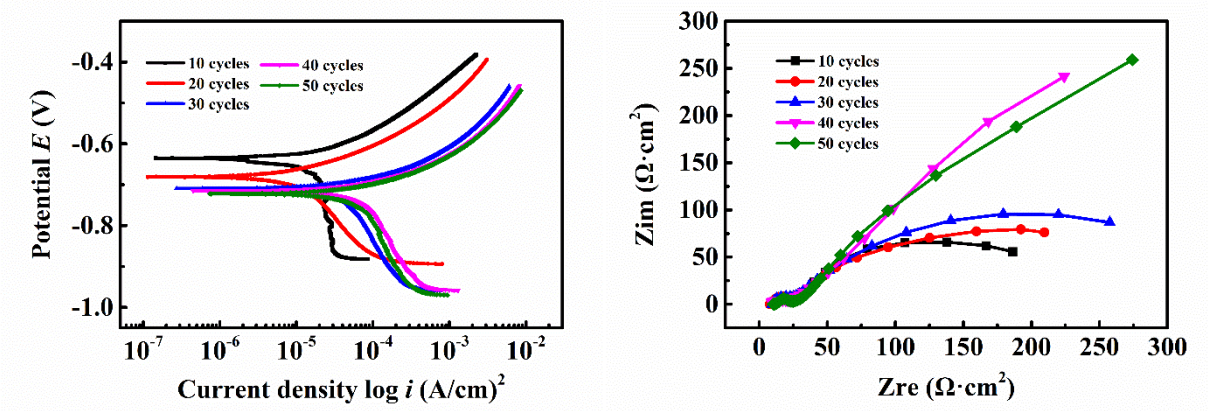

Figure 6. The electrochemical curves including polarization curves and EIS curves of 20MnSi steel under the conditions of T_c = 10-50 cycles in 3 wt.% NaCl solution at 25°C

Table 4. The fitted results of polarization curves of 20MnSi steel under different temperature-alternating cycles

Temperature-alternating cycle	E_{corr} (V)	b_a (mV/dec)	b_c (mV/dec)	I_{corr} (10^{-3} A/m^2)
50	-0.724	69	2350	66.27
40	-0.721	62	2241	60.92
30	-0.718	59	2301	62.84
20	-0.685	73	1461	6.29
10	-0.638	68	705	0.02

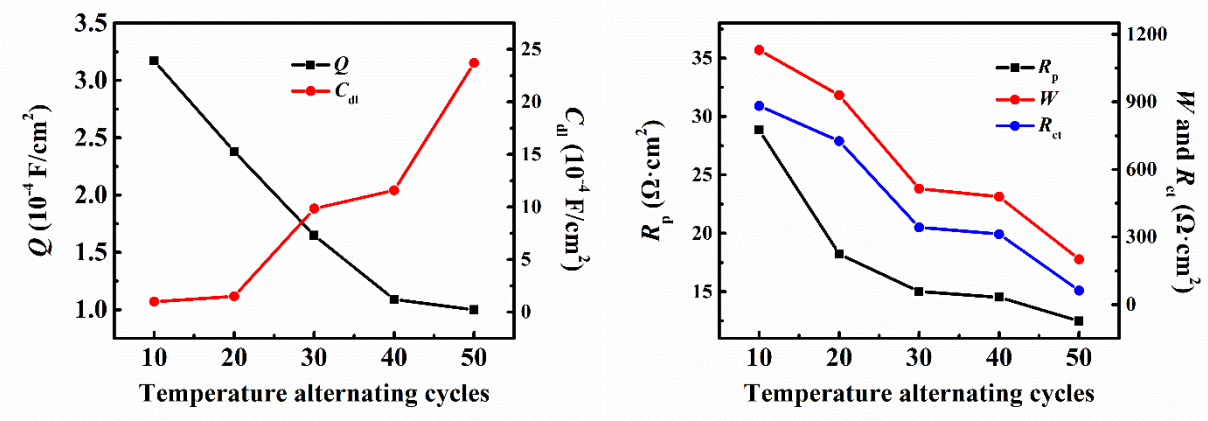

Figure 7. The changes of different EIS parameters, including system capacitance (Q), double-layer capacitance (C_{dl}), surface resistance (R_p), Warsburg resistance (W) and charger transfer resistance (R_{ct}), with temperature-alternating cycles

Table 5. The fitted equations of electrochemical parameters and temperature-alternating cycles

Electrochemical parameter	Fitting equation	R^2
Constant phase Angle element	$Q = -1.431 \cdot \ln(T_c) + 6.524$	0.98
Surface resistance	$R_p = 87.425 \cdot T_c^{-0.502}$	0.97
Warburg resistance	$W = -23.08 \cdot T_c + 1343.5$	0.96
Double-layer capacitance	$C_{dl} = 0.0064 \cdot T_c^{2.062}$	0.91
Charger transfer resistance	$R_{ct} = -20.53 \cdot T_c + 1081.2$	0.95
Corrosion potential	$E_{corr} = -0.056 \cdot \ln(T_c) + 0.515$	0.95

4. CONCLUSIONS

In this paper, the effect of temperature alternation on mechanical properties of embedded reinforcements in rammed earth was investigated through microscopic morphology analysis and electrochemical experiments. The conclusions were drawn as following.

(1) With the increase of the cycles, the yield strength (σ_s) and tensile strength (σ_b) decreased exponentially, the section shrinkage (Ψ) decreased linearly, and the elongation rate (δ) decreased

slowly at first and then rapidly, showing a quadratic function change lawn. Meanwhile, there were obvious yield stages in the stress-strain curve, indicating that the mechanism characteristics of 20MnSi steel changed from plastic to brittle at T_c = 30 cycles.

(2) Temperature alternation destroyed the mesh skeleton structure of 20MnSi steel, and 20MnSi steel precipitated the second phase mainly composed of Ni and Cr element at T_c = 50 cycles.

(3) Temperature alternation mainly affected the cathodic polarization process of 20MnSi steel. With the increase of temperature-alternating cycles, the cathodic process changed from oxygen diffusion control to activation control, while the corrosion potential shifted negatively, and the corrosion current density increased at first and then basically stayed constant. At the same time, the decrease of the three types of resistance (R_p, W and R_{ct}) and the increase of the double-layer capacitance (C_{dl}) indicated that the corrosion resistance of 20MnSi steel decreased.

ACKNOWLEDGEMENTS
This study is supported by the Wuhan City Polytechnic project (2021whcvcC1) and Wuhan Education Bureau project (CXY201814).

References

1. K.C. Shrestha, T. Aoki, M. Miyamoto, P. Wangmo, Pema, J.Y. Zhang and N. Takahashi. *J. Build. Eng.*, 29 (2020) 101179.
2. M. Kosarimovahhed and V. Toufigh. *J. Clean. Prod.*, 277 (2020) 123279.
3. J.C. Reyes, L.E. Yamin, W.M. Hassan, J.D. Sandoval, C.D. Gonzalez and F. A. Galvis. *Eng. Struct.*, 174 (2018) 526.
4. E, Kianfar and V. Toufigh. *Constr. Build. Mater.*, 127 (2016) 884.
5. T.G. Zhou and B. Liu. *Constr. Build. Mater.*, 203 (2019) 567.
6. J. P. Villacreses. J. Granados, B. Caicedo, P. Torres-Rodas and F. Yépez. *Constr. Build. Mater.*, 300 (2021) 124331.
7. T.D. Nguyen, T.T. Bui, A. Limam, T.L. Bui and Q.B. Bui. *J. Build. Eng.*, 43 (2021) 103113.
8. A. Romanazzi, D.V. Oliveira and R.A. Silva. *Constr. Build. Mater.*, 310 (2021) 125228.
9. L.Y. Xie, D. Wang, H.T. Zhao, J.T. Gao and T. Gallo. *J. Archaeolo. Sci.*, 126 (2021) 105303.
10. J.J. Martín-del-Rio, J. Canivell, M. Torres-González, E.J. Mascort-Albea, R. Romero-Hernández, J.M. Alducin-Ochoa and F.J. Alejandre-Sánchez. *J. Build. Eng.*, 44 (2021) 103381.
11. X. Zhang and H. Nowamooz. *Constr. Build. Mater.*, 307 (2021) 124989.
12. F. Ávila, E. Puertas and R. Gallego. *Constr. Build. Mater.*, 325 (2022) 126693.
13. B.V.V. Reddy and R.S.B. Rathod. *J. Build. Eng.*, 49 (2022) 104096.
14. D.M. Ruiz, J.C. Reyes, C. Bran, M. Restrepo, Y.A. Alvarado, N. Barrera, C. Laverde and D. Suesca. *Constr. Build. Mater.*, 320 (2022) 126231.
15. P. Zare, S.S. Narani, M. Abbaspour, A. Fahimifar, S.M.M.M. Hosseini and P. Zare. *Constr. Build. Mater.*, 260 (2020) 120432.
16. Y. Luo, P.S. Zhou, P.P. Ni, X.Q. Peng and J.J. Ye. *Appl. Clay Sci.*, 212 (2021) 106202.
17. Y. Luo, P.S. Zhou, H.H. Ma, P.P. Ni, N. Ding and Y.Y. Xu. *Soil Dyn. Earthq. Eng.*, 145 (2021) 106728.
18. A. Pelé-Peltier, A. Fabbri, J.C. Morel, E. Hamard and M. Lhenry. *Case Stu. Constr. Mat.*, 16 (2022) e00921.
19. M.I. Mota-López, R. Maderuelo-Sanz, J.D. Pastor-Valle, J. M. Meneses-Rodríguez and A. Romero-Casado. *Constr. Build. Mater.*, 273 (2021) 121676.

20. G. Biava, I.B.A.F. Siqueira, R.F. Vaz, G.B. Souza, H.C.M. Jambo, A. Szogyenyi and A.G.M. Pukasiewicz. *Surf. Coat. Tech.*, 438 (2022) 128398.
21. L.Y. Peng, Z.Y. Zhang, J.B. Tan, X.Q. Wu, E.H. Han and W. Ke. *Corros. Sci.*, 198 (2022) 110157.
22. H. Li, W. Liu, L.J. Chen, P.C. Fan, B.J. Dong, Z.H. Ma and T. Wang. *Eng. Fail. Anal.*, 138 (2022) 106297.
23. L.Y. Bai, W.Y. Peng, J. Zhu, X.C. Wu, X.T. Shi, J.H. Xiang, X.H. Deng, Y.Q. Wang, Z.X. Sun and S.Q. Yu. *Corros. Sci.*, 198 (2022) 110139.
24. Z. Li, C.H. Liu, Q.S. Chen, J.J. Yang, J.M. Liu, H.Y. Yang, W. Zhang, R.Q. Zhang, L.X. He, J.P. Long and H. Chang. *Corros. Sci.*, 191 (2021) 109755.
25. T.Y. Ming, H. Xue, T. Zhang, Y.L. Han and Q.J. Peng. *Surf. Coat. Tech.*, 438 (2022) 128420.
26. M.T. de Miguel, M.I. Lasanta, G. García-Martín, R. Díaz and F.J. Pérez. *Corros. Sci.*, 201 (2022) 110274.
27. G.Y. Zhang, Y.F. Zhu, X.M. Lin, Y. Tian, H.L. Ye, X.Y. Jin, N.G. Jin, D.M. Yan, F. Xiao, K.W. Yao and J. Chen. *Constr. Build. Mater.*, 306 (2021) 124873.
28. A.H.E. Moustafa, H.H. Abdel-Rahman, M.K. Awad, A.A.N.A. Naby and S.M. Seleim. Alex. Eng. J., 61 (2022) 2492.
29. M. Liu, S. Bell, M. Segarra, N.H.S. Tay, G. Will, W. Saman and F. Bruno. *Sol. Energ. Mat. Sol. C.,* 170 (2017) 1.
30. A. Strąk, M. Małek, A. Chlanda and E. Sudoł. *J. Build. Eng.*, 50 (2022) 104128.
31. A.M. Oje, A.A. Ogwu, S. Ur Rahman, A.I. Oje and N. Tsendzughul. *Corros. Sci.*, 154 (2019) 28.
32. R.T. Loto. *J. Mater. Res. Technol.*, 8 (2019) 5415.
33. A. Chauhan and U.K. Sharma. *Structures,* 19 (2019) 296.
34. R. Lyons, M. Ing and S. Austin. *Corros. Sci.*, 47 (2005) 413.
35. Q. Li, M.K. Zhao, J. Lin and S.X. Lu. *J. Mater. Res. Technol.*, 15 (2021) 3088.
36.
37. M. Zhang, G.L. Shuai, Y.Q. Wang, Z. Li, D.T. Zhang, H.Z. Yu and L. Li. *Mater. Lett.,* 311 (2022) 131508.
38. S. Guo, Z.Y. Liu, S. Bai, L.N. Ou, J. Zhang, G.Y. He and J.G. Zhao. *J. Alloy. Compd.*, 897 (2022) 163168.